IEEE Access
Multidisciplinary | Rapid Review | Open Access Journal

Received January 11, 2020, accepted January 24, 2020, date of publication January 28, 2020, date of current version February 4, 2020.

*Digital Object Identifier 10.1109/ACCESS.2020.2970086*

# Automatic Process Parameters Tuning and Surface Roughness Estimation for Laser Cleaning

**HAOTING LIU[1], JIACHENG LI[1], YONG YANG[2], JINHUI LAN[1], AND YAFEI XUE[3]**

[1]Beijing Engineering Research Center of Industrial Spectrum Imaging, School of Automation and Electrical Engineering, University of Science and Technology Beijing, Beijing 100083, China
[2]State Key Laboratory of Transient Optics and Photonics, Xi'an Institute of Optics and Precision Mechanics, Chinese Academy of Sciences, Xi'an 710119, China
[3]Guangdong Provincial Key Laboratory of Advanced Welding Technology, Guangdong Welding Institute (China-Ukraine E. O. Paton Institute of Welding), Guangzhou 510650, China

Corresponding author: Yafei Xue (xuebo@protonmail.com)

This work was supported in part by the Fund of State Key Laboratory of Intense Pulsed Radiation Simulation and Effect under Grant SKLIPR1713, in part by the National Natural Science Foundation of China under Grant 61975011, and in part by the Fundamental Research Fund for the China Central Universities of USTB under Grant FRF-BD-19-002A.

**ABSTRACT** An image analysis-based two-stage process parameters tuning and Surface Roughness (SR) estimation algorithm is proposed for the laser cleaning application. A Cartesian coordinate robot is utilized to collect image and implement cleaning. Before cleaning, in order to tune the proper laser parameters, first, the environment lighting is controlled for the metal image collection. Second, lots of classification features are computed for the images above. The Gray-Level Co-occurrence Matrix (GLCM) texture features, the concavo-convex region features, the histogram symmetry difference feature, and the imaging thermophysical property features are computed. Third, the initial laser parameters are created randomly and an iteration computation is performed: a Support Vector Machine (SVM) is used to forecast the cleaning effect; its inputs include the classification features and the initial laser parameters; its output is the cleaning effect degree. If the SVM output cannot fulfill user's demand, the laser parameters will be updated randomly. This iteration will be implemented constantly until the SVM output becomes valid. Then the laser cleaning will be performed. When estimating SR for the cleaned metal, multiple image features are calculated for the images after cleaning. The features include the Tamura coarseness, some GLCM features, and the convex region feature. To improve the prediction precision, different feature combinations are used for different cleaning effects. The linear function and the 3-order polynomial function are considered for the SR estimation. After tests, the accuracies of SVM, the SR prediction function, and the integrated SR control and estimation algorithm can be 90.0%, 80.0% and 80.0% approximately.

**INDEX TERMS** Laser cleaning, process parameters, surface roughness, image feature, thermophysical property.

## I. INTRODUCTION

The laser cleaning can remove the reminders in the surface of workpiece by the principles [1] of mechanic resonance, thermal expansion, or evaporation and gasification processes, etc. Comparing with other cleaning techniques, such as the mechanical cleaning [2], the chemical cleaning [3], or the ultrasonic cleaning [4], the laser cleaning has lots of merits such as the small contamination, the convenient control, and the comparable low application cost. Generally speaking, the laser cleaning includes the dry cleaning [5] and the steam cleaning [6]. The former eliminates the reminders by changing the physical states of particles on the surface of workpiece and conquering their adhesive forces; while the latter removes the reminders by gasifying the injected surface liquid which can take away the redundant particles. Because of the advancements of the optoelectronics and the computer techniques, the laser cleaning has met its great developments [7] in recent years.

Many indices can be used to evaluate the processing effect of laser cleaning, the Surface Roughness (SR) [8] is one of them. The SR can reflect the smoothness degree of

The associate editor coordinating the review of this manuscript and approving it for publication was Utku Kose.

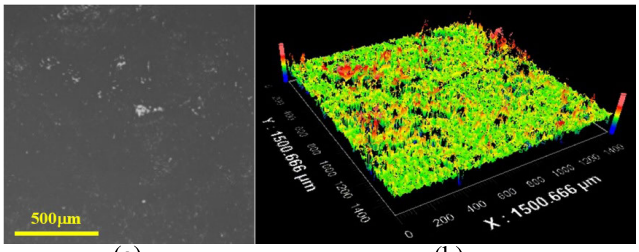


**FIGURE 1.** The 2D and 3D image samples of a kind of carbon steel: (a) is the 2D gray image of carbon steel; and (b) is the colored 3D profile of (a).

material surface. It can affect the fitting property, the wearability, or the contact stiffness among workpieces. Many methods have been developed to measure SR including the contact technique and the noncontact measurement. The contact technique uses a probe [9] to percept the surface topography change of the workpiece; while the noncontact measurement employs the optic approach together with some mathematical or physical models [10] to estimate the SR. Obviously, the latter method has lots of advantages including the high precision, the low possibility of substrate destructiveness, and the excellent measurement stability and repeatability. As a kind of noncontact method, the image analysis-based SR estimation [11] gets great notice in recent years.

Regarding the laser cleaning, it will be helpful if the SR after cleaning can be estimated by the analysis result of 2D image automatically and precisely. Fig. 1 shows the 2D and the 3D images of a carbon steel. In Fig. 1, (a) is the 2D gray image, and (b) is the colored 3D profile of (a) which is measured by a white-light interferometer. Comparing with the 3D profile, many factors will affect the measurement precision of 2D image. First, the metal color and texture will create apparent influences on image analysis. For example, some white islands can be observed: parts of them come from the small hole or salient in substrate; while others are the texture colors of metal itself. Second, the photography conditions, including the environment light [12], the camera performance, and the observation distance, etc. will also affect the imaging results. Third, the corrosive components [13] which cover the surface of substrate are another factor.

Many studies have been done to solve the image analysis-based SR estimation. In [14], the Gray-Level Co-occurrence Matrix (GLCM) was employed to estimate the SR of brittle graphite. In [15], five image edge detection methods were considered to evaluate SR. The Laplacian of Gaussian method was found to be the best solution. In [16], the RGBD camera was used for materials recognition and SR estimation. After the survey of lots of related works, it can be found the current researches can realize the SR estimation by using the observed image directly; however, it will be great useful if the SR can be controlled and estimated [17] before laser cleaning. That means even a corrosion layer covers the substrate we hope to control and estimate SR of substrate before the exfoliation of corrosion layer. Clearly, to achieve that target, both the control of laser process parameters and the analysis of cleaned image should be implemented.

In this paper an image analysis-based two-stage processing algorithm is developed to control and forecast the SR for laser cleaning application. A Cartesian coordinate robot [18] is used to implement the cleaning and photography tasks. Our procedures include the laser process parameters tuning before cleaning and the SR prediction after cleaning. When realizing the former procedure, after the environment lighting control, the Support Vector Machine (SVM) [19] is employed. Its inputs include the laser process parameters, some traditional and new defined image features, and the imaging thermophysical property features [20]. Its output is the cleaning effect degree, i.e., the classification degree of SR. An iteration computation is carried out to find the proper laser parameters. When carrying out the latter estimation, different image features are used for the images with different cleaning effects. Both the linear function and the 3-order polynomial function are used for the SR estimation.

The main contributions of this paper include: first, an integrated control and estimation algorithm of SR for laser cleaning is developed. In contrast to the traditional SR measurement methods which can only be used after cleaning, our proposed technique can control the SR before and during the cleaning. Second, a kind of intelligent tuning algorithm of the multiple laser process parameters is proposed. A SVM-based iterative computation is developed to search the proper laser parameters. Third, lots of new imaging features are defined. The concavo-convex region features, the histogram symmetry difference feature, and the imaging thermophysical property features are all designed for this application.

In the following section, first the laser cleaning issue will be presented. Second the proposed computational method will be shown. Third some experiment results will be given.

## II. LASER CLEANING TECHNIQUE AND ITS EFFECT ON SURFACE ROUGHNESS

### A. APPLICATION DEFINITION AND ITS PROPOSED HARDWARE SOLUTION

This paper focuses on the laser cleaning application of a kind of marine carbon steel which works in a stable nature state. Here the ''stable nature state'' means this carbon steel will not be pressed, worn, or scrubbed during its service period. It will not experience the extreme high or low temperature. Only the seawater, the sun light, and the nature wind affect it. Thus the main effect result of external environment on its surface is the metal corrosion problem [21]. Another assumption is that the material stability [22] of carbon steel is comparable high after it leaves its manufacturing factory. After all the manufacturers have to guarantee their product qualities [23]. That indicates the thermophysical property parameters and the surface performance of carbon steel are stable. Finally, regarding the laser cleaning issue, we suppose the SR is mainly related to its initial metal corrosion state and the corresponding laser cleaning effect.

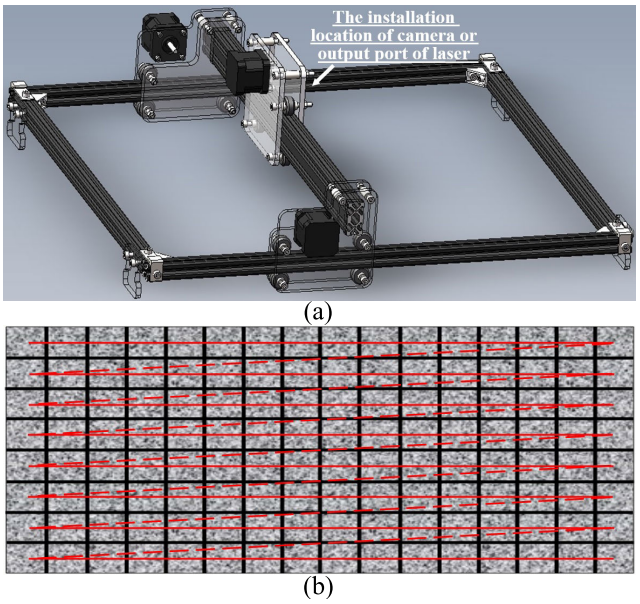


**FIGURE 2.** The schematic diagrams of the Cartesian coordinate robot and its working path: (a) is the schematic diagram of the Cartesian coordinate robot; (b) shows its working path.

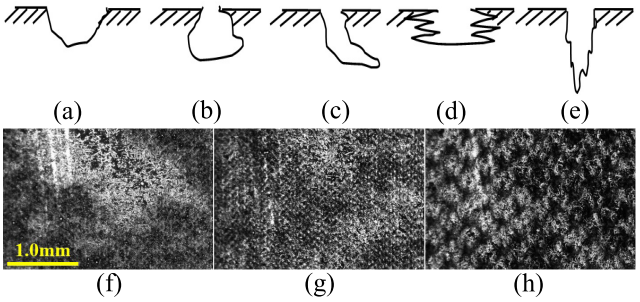


**FIGURE 3.** The metal corrosion schematic diagrams and examples: (a) to (e) are the schematic diagrams of the metal corrosion problem; (f) to (h) are the practical photos of the corrosive metal.

A Cartesian coordinate robot is used to implement the laser cleaning. Fig. 2 shows its structure and working path schematic diagrams. Currently, because of the limited working space, a camera and a laser output end can be fixed in this system alternately. When it works, first, a workpiece will be put under the robot. Second, this system will take the camera to implement the image capture task along the red path: the solid lines mark its working path; while the dash lines show the motion but non-working path of that camera. The black grids present the photography regions. Third, after the image capture, a series of imaging features will be computed and the laser process parameters will be created intelligently. Fourth, this system will take the output port of laser to carry out the cleaning task. The same working path in (b) will be used. Finally, the camera system will be used again to collect image after cleaning and estimate the SR.

### B. METAL CORRSION AND ITS EFFECT ON SR

The corrosion will affect the SR definitely. Fig. 3 shows the examples of metal corrosion: (a) and (b) may come from the integrated erosion of rain, wind, and sun light; (c) may be derived from the sustained drops of water; (d) and (e) may be created by the high salinity seawater; (f) to (h) are the actual gray images of the corrosion metal. Many indices [24] have been proposed for SR computation, such as the mean surface height index $Sa$ or the root mean square height index $Sq$, etc. In this paper we only consider the index $Sa$; its computational formula is shown in (1). From Fig. 3, the image can surely represent the SR to some extent. Although lots of colors and textures exist in the metal surface; however, some gullies and humps can still be observed from the image: the gully may behave as a black region; while the hump may present as a white block in image. Thus the effective image features should be designed when estimating the SR.

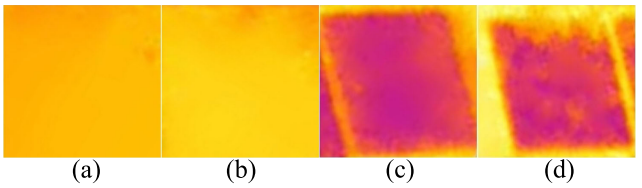


**FIGURE 4.** The infrared thermography samples of laser cleaning: (a) and (b) are the infrared thermography images before laser cleaning; (c) and (d) are the corresponding images after cleaning.

$$Sa = \frac{1}{n_x n_y} \sum_{i=1}^{n_x} \sum_{j=1}^{n_y} \left| \eta \left( x_i, y_j \right) \right| \tag{1}$$

where $n_x$ and $n_y$ are the amounts of sample point in the user defined $x$ and $y$ coordinate axes in workpiece, respectively; $\eta(x_i, y_j)$ represents the centered height in position $(x_i, y_j)$, where the mean height calculated on the definition area has been already subtracted from that height.

### C. THERMAL EFFECT AND ITS INFLUENCE ON SR

In this paper, a pulse fiber laser is used to carry out the cleaning task. Its cleaning principle is mainly related to the thermal effect [25]. Fig. 4 shows the infrared thermography samples of laser cleaning. In Fig. 4, (a) and (b) are the images which do not experience the laser cleaning; (c) and (d) are the results which have went through the cleaning. The rectangle cleaning regions are shown here. From Fig.4, the infrared images do not have too many differences in imaging intensity before cleaning; however, if the laser acts on the metal surface, the diversities of surface profile can be observed clearly: the uneven thermal effect can be identified from these images because of the metal corrosion. The differential equation of thermal field [26] is shown in equation (2). From (2), the material thermophysical properties can influence the processing effect of laser cleaning; thus it is necessary to build some computational indices for them from the image processing point of view.

$$\rho c \frac{\partial T}{\partial t} = k_x \frac{\partial^2 T}{\partial x^2} + k_y \frac{\partial^2 T}{\partial y^2} + k_z \frac{\partial^2 T}{\partial z^2} + w\left(x, y, z; t\right) \tag{2}$$

where $\rho$ is the material density; $c$ is the specific heat capacity of material; $k_x$, $k_y$, and $k_z$ are the thermal conductivity of material in $x$, $y$, and $z$ directions; $T$ is the temperature;

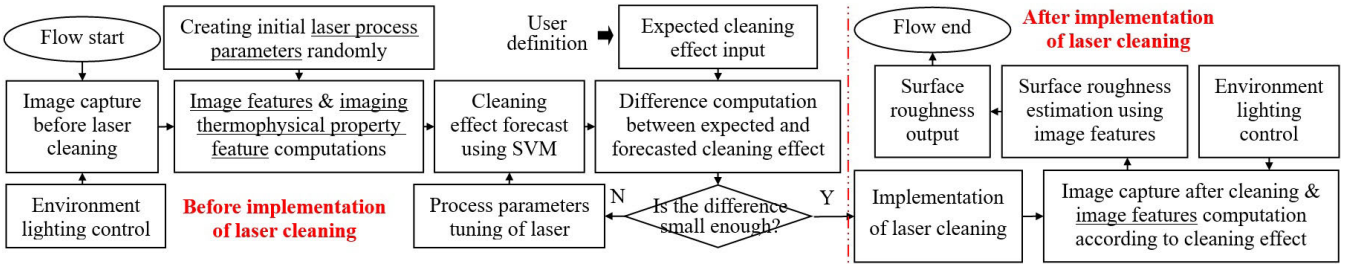


**FIGURE 5.** The proposed implementation flow chart of the laser process parameters tuning and the SR estimation algorithm.

$w(x, y, z; t)$ is a heat source function, and $t$ is the observation time.

## III. PROPOSED SURFACE ROUGHNESS CONTROL AND FORECAST ALGORITHM

### A. PROPSED PROCESSING FLOW CHART

Fig. 5 shows the proposed processing flow chart of the laser process parameters tuning and the SR estimation.

- First stage: the laser parameters tuning before cleaning

Before cleaning, the process parameters of laser should be estimated to fulfill the cleaning effect demand of user, i.e., the expected SR scope. First, the environment lighting will be controlled to get the proper images. Second, both the image [27] and the imaging thermophysical property features will be computed for the captured images. Third, the initial laser parameters will be set randomly and an iteration computation [28] will be carried out. A SVM is used to predict the cleaning effect: its inputs include the image features, the imaging thermophysical property features, and the initial laser parameters; its output is the cleaning effect. If its output cannot fulfill the user requirement, the new laser parameters will be created randomly. This iteration will be repeated constantly until the SVM output becomes valid.

- Second stage: the SR estimation after cleaning

After the implementation of the controlled laser cleaning, the metal surface attribution will approach to the expected processing effect, then the SR will be estimated. Multiple image features, such as the GLCM features or the Tamura coarseness [29] will be computed for the image after cleaning. The environment lighting control will also be performed. Then the SR can be predicted by using the features above. To improve the prediction precision, different feature combinations are used for the images with different cleaning effects which are gotten in the first stage. Both the linear and the polynomial functions are utilized for SR prediction.

### B. ENVIRONMENT LIGHTING CONTROL METHOD

Multiple image features will be computed in this paper to control the laser process parameters and estimate the SR. It is well known the photography effect of visible light camera will be influenced by the environment light seriously. Thus to decrease the negative effect of environment light, a lighting compensation method is designed. Both a standard color card and a Light Emitting Diode (LED) light source are used to provide a reference and make the light compensation [30] for our system. The distributed surface light source or the ringing shape light source can be used. The light source should realize the continuous intensity tuning function. The color card is used here to provide a reference for the environment light identification of metal surface. For the sake of simpleness, the white color card is used. It also should be emphasized that the color card is needed to have the low light reflection attribution; otherwise the high light reflection region can be observed in the camera vision field which will influence the color perception effect of our system seriously.

The specific implementations of lighting compensation are presented below. First a white color card is put near the corrosion metal. Second, the camera will take photos of both the corrosion metal and that color card. Third, the camera will read the pixel intensity of that color card and compare it with the standard intensity of white color card which is stored in the memory of our system in advance. The standard intensity of white color card indicates a proper environment light condition for the image capture; and it also represents a valid pixel intensity response. Clearly, the computed image features will be qualified under this standard environment light. Fourth, if the offset between the collected pixel intensity and the standard pixel intensity of white color card is large than a threshold, a traversing outputs of LED light source will be performed until the offset becomes small enough. Then the image features will be computed. Lastly, this environment lighting control method can guarantee the computational stability of image feature to some extent.

### C. PRELIMINARY CONTROL OF CLEANING EFFECT

The SVM is used to search the proper laser parameters. Its inputs have the image features, the imaging thermophysical property features, and the laser parameters. Table 1 shows the list of them. The image features include the GLCM feature vector, the concavo-convex region feature vector, and the histogram feature. Regarding GLCM, the angular second moment $M_{GLCM\_ASM}$, the entropy $M_{GLCM\_ENT}$, the contrast $M_{GLCM\_CON}$, the inverse differential moment $M_{GLCM\_IDM}$, and the correlation $M_{GLCM\_COR}$ are computed; the directions of 0°, 45°, 90°, and 135° are all investigated. The concavo-convex region feature vector $M_{CCR}$ has the concavo

**TABLE 1. Training Data List of SVM.**

| Num | Feature name |
|---|---|
| 1 | The feature vector of GLCM $M_{GLCM}$=[$M_{GLCM\_ASM}$, $M_{GLCM\_ENT}$, $M_{GLCM\_CON}$, $M_{GLCM\_IDM}$, $M_{GLCM\_COR}$]=[$M_{G\_ASM\_0}$, $M_{G\_ASM\_45}$, $M_{G\_ASM\_90}$, $M_{G\_ASM\_135}$, $M_{G\_ENT\_0}$, $M_{G\_ENT\_45}$, $M_{G\_ENT\_90}$, $M_{G\_ENT\_135}$, $M_{G\_CON\_0}$, $M_{G\_CON\_45}$, $M_{G\_CON\_90}$, $M_{G\_CON\_135}$, $M_{G\_IDM\_0}$, $M_{G\_IDM\_45}$, $M_{G\_IDM\_90}$, $M_{G\_IDM\_135}$, $M_{G\_COR\_0}$, $M_{G\_COR\_45}$, $M_{G\_COR\_90}$, $M_{G\_COR\_135}$] |
| 2 | The feature vector of concavo-convex region $M_{CCR}$=[$M_{CCR\_0}$, $M_{CCR\_1}$] |
| 3 | The feature of histogram symmetry difference $M_{HSD}$ |
| 4 | The feature vector of imaging thermophysical property $M_{ITP}$=[$M_{ITP\_GI}$, $M_{ITP\_TEM}$] |
| 5 | The process parameter vector of laser $M_{LPP}$=[$M_{LPP\_P}$, $M_{LPP\_LV}$, $M_{LPP\_LS}$] |

region feature $M_{CCR\_0}$ and the convex region feature $M_{CCR\_1}$. The histogram feature is the histogram symmetry difference $M_{HSD}$. The imaging thermophysical property feature vector $M_{ITP}$ can reflect the material characteristics. It includes the typical corrosion gray intensity $M_{ITP\_GI}$ and the maximum cleaning temperature $M_{ITP\_TEM}$. The laser parameters are the power $M_{LPP\_P}$, the linear velocity $M_{LPP\_LV}$, and the line space $M_{LPP\_LS}$.

Regarding the image features, first, the GLCM features [31] are computed. Obviously, they can represent the texture information of corrosive metal. Second, the concavo-convex region features are defined. They can indicate the typical texture spots in metal surface. Equations (3) and (4), (5) and (6) show their computational methods. The concavo regions mainly are some holes or crevices. They appear in the surface of workpiece as pixel bunches with deep color. The convex regions may be some corrosion parts or burrs in metal surface. They can be looked on as some pixel bunches with light color. When designing the computational method of them, the threshold segmentation technique is considered.

$$M_{CCR\_0} = \frac{1}{f_{sum}} \sum_{i=1}^{N} \sum_{j=1}^{M} f_{b\_0}(i,j) \tag{3}$$

$$f_{b\_0}(i,j) = \begin{cases} 1 & f(i,j) < T_0 \\ 0 & else \end{cases} \tag{4}$$

$$M_{CCR\_1} = \frac{1}{f_{sum}} \sum_{i=1}^{N} \sum_{j=1}^{M} f_{b\_1}(i,j) \tag{5}$$

$$f_{b\_1}(i,j) = \begin{cases} 1 & f(i,j) > T_1 \\ 0 & else \end{cases} \tag{6}$$

where $f(i,j)$ is the pixel intensity in image position $(i,j)$; $M$ and $N$ are the image width and the height; $f_{sum}$ is the pixel intensity sum of whole image; $f_{b\_0}(i,j)$ and $f_{b\_1}(i,j)$ are the segmentation results of original image $f(i,j)$; $T_0$ and $T_1$ are the segmentation thresholds.

Third, a histogram feature is designed. Fig. 6 shows the histograms and their sketch maps before and after cleaning. In Fig. 6, (a) and (b) are the actual histograms before and after cleaning; and (c) and (d) are the sketch maps of (a) and (b), respectively. From Fig. 6, the symmetry of

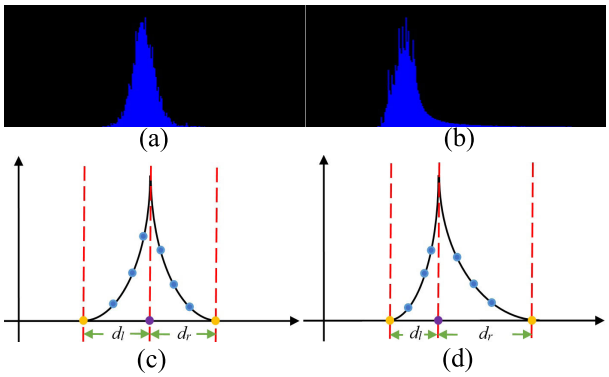


**FIGURE 6. The histograms and their sketch maps before and after laser cleaning: (a) and (b) are the actual histogram samples before and after laser cleaning; (c) and (d) show the sketch maps of (a) and (b), respectively.**

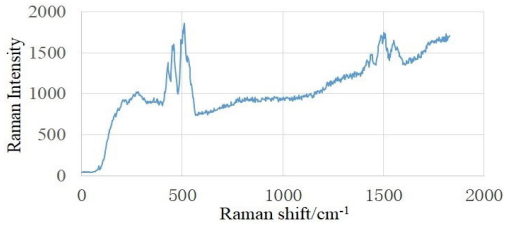


**FIGURE 7. The original Raman spectrum example before laser cleaning.**

histogram is good before cleaning; however an offset happens after cleaning. This is mainly because the corrosion is almost uniform-distributed in the metal surface before cleaning; while the non-uniform metal texture can be observed after cleaning. Equation (7) shows its computational method. The maximum value point of histogram can always be found easily; however the positions of its two intersection points are difficult to estimate because of the histogram variety. To solve that problem, first the points (the blue points in Fig. 6 (c) and (d)) near the maximum value point in certain direction are selected randomly, then the fitting method of the polynomial function is used to find their interaction point (the yellow points).

$$M_{HSD} = |d_l - d_r| \tag{7}$$

where $d_l$ is the width between the perpendicular line of the maximum value data and the left intersection point; $d_r$ is the width between the perpendicular line of the maximum value data and the right intersection point (see Fig. 6 (c) and (d)).

When designing the imaging thermophysical property features, both the typical corrosion color and the maximum cleaning temperature are considered. When computing the typical corrosion color, first, the Raman spectrum [32] is used to estimate the main components and their contents of corrosion layer. Fig. 7 shows the examples of Raman spectrum. Second, the multiple oxides, such as $Fe_2O_3$ and $Fe_3O_4$, are mixed together to generate the typical corrosion components. Clearly, the mixture components and their contents are derived from the analysis results of Raman spectrum. Third, the mixtures above are scattered in a polished metal substrate randomly; then lots images can be captured. Lastly, the image gray intensity distributions of mixtures will

be computed. This kind of distribution can be regarded as an imaging thermophysical property feature. The gray intensity of corrosion component can be computed by (8); and its image feature $M_{IPT\_GI}$ can be defined by (9).

$$M_{ITP\_AVE} = \frac{1}{MN}\sum_{i=1}^{N}\sum_{j=1}^{M} f(i,j) \tag{8}$$

$$M_{ITP\_GI} = \begin{cases} 1 & M_{ITP\_AVG} \in [T_{ITP}^{0}, T_{ITP}^{1}] \\ 2 & M_{ITP\_AVG} \in [T_{ITP}^{1}, T_{ITP}^{2}] \\ \ldots & \ldots \\ n & M_{ITP\_AVG} \in [T_{ITP}^{n-1}, T_{ITP}^{n}] \end{cases} \tag{9}$$

where $M_{ITP\_AVE}$ is the intensity average of image $f(i,j)$, $M$ and $N$ are the image width and the height; $T_{ITP}^{k}$ $(k = 0, 1, \ldots, \mathrm{n})$ is the intensity threshold which is decided by the Raman spectrum; and $n$ is the type token of typical corrosion color.

Regarding the maximum laser cleaning temperature, a simulation-based method is used to estimate its value. First, a 3D model of corrosion metal is built. This model has a corrosion layer and a metal substrate layer. Before the implementation of simulation, the thermophysical property parameters of both the corrosion and the substrate layers should be set properly. Second, a pulse fiber laser is simulated to clean the corrosion layer for the model above. A series of laser process parameters can be set in this simulation including the linear velocity, the power, the frequency, the pulse width, the single pulse energy, the focal length, and the line space. Third, the cleaning temperature can be estimated by equation (10). The finite element analysis method [33] can be utilized here. Because the temperature simulation will be carried out consecutively in both the time dimension and the space dimension; its global maximum value can be selected during that simulation. Then the maximum cleaning temperature will be defined by (11).

$$\rho C_p \frac{\partial T}{\partial t} + \rho C_p u \cdot \nabla T + \nabla \cdot (-k \nabla T) = Q \tag{10}$$

$$M_{ITP\_TEM} = \max_{i \in [1, N_{TEM}]} \{T_i\} \tag{11}$$

where $\rho$ is the material density; $C_p$ is the heat capacity at constant pressure; $T$ is the cleaning temperature; $t$ means the simulation time; $u$ is the laser scanning speed; $k$ is the heat transfer coefficient; $Q$ is the laser heat flux; $\nabla$ is the gradient operator; $T_i$ is the $i^{\text{th}}$ observation of the consecutive cleaning temperature $T$; $N_{TEM}$ is the maximum observation times; the function $\max\{^*\}$ realizes the maximum value computation.

After the input vector of SVM is calculated, its output data should be defined. In this paper, the cleaning effect is looked on as the supervising data. Currently, the cleaning effect is defined by the SR, i.e., the $Sa$. Without loss of generality, the cleaning effect is classified into 3 degrees. That means the $Sa$ should be segmented into 3 independent intensity regions. After the definition of SVM, an iteration computation is used to find the proper values of laser parameters: the initial parameters of laser are given randomly, then the SVM will compute a prediction result of the cleaning effect. After that a distance will be computed between the user expected output and the predicted cleaning effect above. Equation (12) shows the computational method. If the distance is smaller than a threshold, the SVM computation will be terminated; otherwise the new random values of laser parameters will be created. Regarding the SVM, the polynomial kernel function in (13) is used because of its good computational effect.

**TABLE 2. The image features and the prediction methods for SR estimation under Different Cleaning Effects.**

| Cleaning effect degree | Image feature | Prediction method |
|---|---|---|
| 1 | $[M_{T\_Coa}]$, $[M_{CCR\_1}]$ | Linear function, 3-order polynomial function |
| 2 | $[M_{CCR\_1}]$, $[M_{G\ COR}^{AVE}]$ | 3-order polynomial function |
| 3 | $[M_{G\ COR}^{AVE}]$ | 3-order polynomial function |

$$O_{SVM} = \begin{cases} 1 & abs\left(O_{SVM}^{com} - O_{SVM}^{user}\right) \le T_{O}^{SVM} \\ 0 & else \end{cases} \tag{12}$$

$$K\left(x_i, x_j\right) = \left(\gamma x_i^T x_j + r\right)^d \tag{13}$$

where $O_{SVM}^{com}$ is the predicted result of SVM; $O_{SVM}^{user}$ is the expected output of user; $T_{O}^{SVM}$ is a threshold; $O_{SVM}$ is the output of our system; $K(^*)$ is the kernel function; $x_i$ and $x_j$ are the training data; $\gamma$ is a weight; $r$ and $d$ are control parameters, and $\gamma = 0.9$, $r = 0.0$, and $d = 3$ in this paper.

### D. ELABORATED ESIMATION OF SR

After the tuning of laser parameters the practical cleaning operation will be performed. Then the SR can be controlled to approach the cleaning requirement of system user. Because of the existence of corrosion layer, it will be unreliable to use the image data before cleaning to predict the SR after cleaning. Clearly, it is almost impossible to estimate the corrosion thickness and its accurate distribution just using the visible light image [34]. Thus the image capture after cleaning and the corresponding image feature analysis are necessary. Since three types of cleaning effect can be achieved, our following mission is to design the image features and their prediction methods for the images which have different cleaning effects.

Table 2 shows the image features and the prediction methods of SR estimation under different cleaning effects. Lots of image features are compared, including the GLCM features, the Tamura feature, the Local Binary Pattern (LBP) features [35], etc. Table 2 shows the best results in our experiment. First, regarding the cleaning effect in rank 1, both the Tamura coarseness and the convex region feature are used. The computational method of Tamura coarseness is shown in (14) and (15). Second, as for the cleaning effect in rank 2, the average of the GLCM correlation $M_{GLCM\_COR}$ is computed. Its definition can be found in (16). Before estimating the GLCM, a preprocessing is performed: after the histogram equalization we compute the intensity sum of the whole image and use the intensity of each pixel to divide that

sum to get a new image. Third, when it comes to the cleaning effect in rank 3, the feature $M^{AVE}_{G\_COR}$ is used again.

$$M_{T\_Coa} = \frac{1}{M \times N} \sum_{i=1}^{M} \sum_{j=1}^{N} S_{opt}(i,j) \tag{14}$$

$$S_{opt}(i,j) = 2^k \tag{15}$$

$$M^{AVE}_{G\_*} = \frac{1}{4} \begin{pmatrix} M_{G\_*\_0} + M_{G\_*\_45} \\ + M_{G\_*\_90} + M_{G\_*\_135} \end{pmatrix} \tag{16}$$

where $S_{opt}(i, j)$ is an optimal function of each pixel in $(i, j)$ when $k$ can maximize the average intensity difference in the horizontal and the vertical directions, $k = 3$; $M$ and $N$ are the width and the height of image block; and symbol "*" can be set by *ASM*, *ENT*, *CON*, *IDM*, and *COR* (see Table 1).

Table 2 also shows the prediction methods of SR under different cleaning effects. In Table 2, regarding the cleaning effect in rank 1, both the linear and the 3-order polynomial functions can get the same prediction result for their respective image features $[M_{T\_Coa}]$ and $[M_{CCR\_1}]$. As for the cleaning effects in rank 2 and rank 3, the 3-order polynomial function can get the best prediction result. Equations (17) and (18) show the computational methods of the linear function and the 3-order polynomial function. Other prediction methods, such as the Support Vector Regression (SVR) [36] and the n-order (n≠3) polynomial functions etc., are also considered here. However, we do not use them for their limited computational effects in our experiment in the end.

$$y = ax + b \tag{17}$$

$$y = c_0 + c_1 x + c_2 x^2 + c_3 x^3 \tag{18}$$

where $x$ represents the input image feature; $y$ is the estimation result of SR; $a$, $b$, $c_0$, $c_1$, $c_2$, and $c_3$ are estimated parameters.

## IV. EXPERIMENTS AND DISCUSSIONS

A series of experiments are performed to evaluate the correctness of our method. All the programs are developed by C code on our PC (4.0 GB RAM, 1.70GHz CPU).

### A. EXPERIMENTAL SYSTEM AND DATA

Fig. 8 shows the proposed experiment system and the corresponding image data. In Fig. 8, (a) is the photo of the Cartesian coordinate robot; (b) and (c) are the photos of the visible light camera and the laser output end, respectively; (d) and (e) are the photos of the captured image samples before and after cleaning. When this system works, the camera and the output port of laser will be installed in the Cartesian coordinate robot alternatively. In Fig. 8, a coordinate system is defined in the Cartesian coordinate robot (the red coordinate axes in (a)): the same electric motors are used for this robot, thus the motion speeds of camera or laser output end in both the x axis and the y axis are same. From Fig. 8, the imaging appearances before and after laser cleaning have the distinct differences in both the pixel intensity and the texture feature. Thus it is possible to use these information to control the laser output effect and forecast the SR. Tables 3, 4, and 5 show the basic parameters of the Cartesian coordinate robot, the visible light camera, and the laser, respectively. Table 6 also presents the carbon steel components in this research.

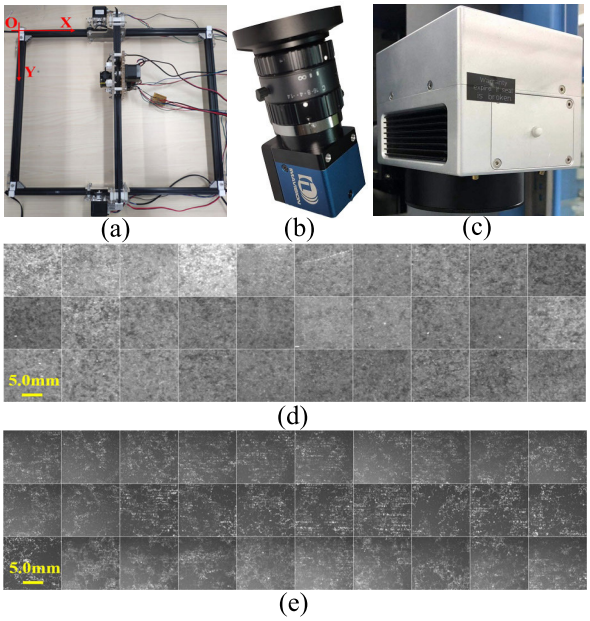


**FIGURE 8.** The experiment system and the image samples: (a) is the photo of the Cartesian coordinate robot; (b) presents the photo of the visible light camera; (c) shows the photo of the laser output end; and (d) and (e) illustrate the photos of the captured image samples before and after cleaning.

**TABLE 3.** The basic parameters of cartesian coordinate robot.

| Size (cm×cm) | Maximum motor rotation speed (rpm) | The re-orientation accuracy (mm) |
|---|---|---|
| 60×50 | ≤1200 (x axis and y axis) | ±0.01 (x axis and y axis) |

**TABLE 4.** The basic parameters of visible light camera.

| Sensor type | Sensor size (μm) | Maximum resolution |
|---|---|---|
| CMOS | 3.2×3.2 | 2048×1536 |
| Focal length (mm) | Frame rate (Hz) | Working wavelength |
| 5.0 | 12 | Visible light |

**TABLE 5.** The basic parameters of laser.

| Linear velocity (mm/s) | Maximum average output power (W) | Frequency (kHz) | Pulse width (ns) |
|---|---|---|---|
| 100~7000 | 190~210 | 20~50 | 30~400 |
| Single pulse energy (mJ) | Focal length (mm) | Line space (mm) | Times of cleaning |
| 1.5~10.5 | 217~227 | 0.02~1.0 | 1 |

**TABLE 6.** The components of a kind of carbon steel.

| C | Si | Mn | S | P | Fe |
|---|---|---|---|---|---|
| 0.14 | 0.13 | 0.44 | 0.031 | 0.015 | 0.244 |

### B. EVALUATION OF LIGHTING CONTROL METHOD

Fig. 9 shows the examples of the LED light source and the corrosive metals with the color cards under different lighting conditions. An experiment is performed to evaluate the

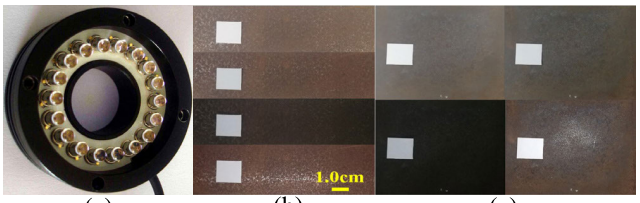


**FIGURE 9.** The application examples of LED light source and color card: (a) is the photo of the LED light source; (b) and (c) are the photos of the corrosive metals with the color cards under different lighting conditions.

**TABLE 7.** The image feature comparisons before and after the application of lighting compensation method.

| Data | $M_{G\_ASM\_0}$ | $M_{G\_ASM\_45}$ | $M_{G\_ASM\_90}$ | $M_{G\_ASM\_135}$ | $M_{G\_ENT\_0}$ |
|---|---|---|---|---|---|
| A | 0.225988 | 0.205106 | 0.223746 | 0.204001 | 1.87767 |
| B | 0.204948 | 0.18456 | 0.204859 | 0.183244 | 1.90279 |
| A′ | 0.279537 | 0.259525 | 0.278578 | 0.259402 | 1.87738 |
| B′ | 0.219406 | 0.199657 | 0.218083 | 0.199357 | 2.02088 |
| C | 0.278446 | 0.258619 | 0.277959 | 0.258942 | 1.88171 |
| \|A-C\| | 0.052458 | 0.053513 | 0.054213 | 0.054941 | 0.00404 |
| \|A′-C\| | ***0.001091*** | ***0.000906*** | ***0.000619*** | ***0.00046*** | 0.00433 |
| \|B-C\| | 0.073498 | 0.074059 | 0.0731 | 0.075698 | 0.02108 |
| \|B′-C\| | ***0.05904*** | ***0.058962*** | ***0.059876*** | ***0.059585*** | 0.13917 |
| Data | $M_{G\_ENT\_45}$ | $M_{G\_ENT\_90}$ | $M_{G\_ENT\_135}$ | $M_{G\_CON\_0}$ | $M_{G\_CON\_45}$ |
| A | 1.9827 | 1.88869 | 1.98891 | 0.199376 | 0.26196 |
| B | 2.00481 | 1.9025 | 2.01066 | 0.217141 | 0.281978 |
| A′ | 1.96914 | 1.87423 | 1.96965 | 0.295237 | 0.379775 |
| B′ | 2.11414 | 2.01982 | 2.11625 | 0.352279 | 0.448164 |
| C | 1.97442 | 1.8786 | 1.9725 | 0.29245 | 0.378097 |
| \|A-C\| | 0.00828 | 0.01009 | 0.01641 | 0.093074 | 0.116137 |
| \|A′-C\| | ***0.00528*** | ***0.00437*** | ***0.00285*** | ***0.002787*** | ***0.001678*** |
| \|B-C\| | 0.03039 | 0.0239 | 0.03816 | 0.075309 | 0.096119 |
| \|B′-C\| | 0.13972 | 0.14122 | 0.14375 | ***0.059829*** | ***0.070067*** |
| Data | $M_{G\_CON\_90}$ | $M_{G\_CON\_135}$ | $M_{G\_IDM\_0}$ | $M_{G\_IDM\_45}$ | $M_{G\_IDM\_90}$ |
| A | 0.204773 | 0.26662 | 0.903969 | 0.876986 | 0.901457 |
| B | 0.216743 | 0.286162 | 0.895469 | 0.868482 | 0.895543 |
| A′ | 0.286142 | 0.378553 | 0.871794 | 0.845405 | 0.872379 |
| B′ | 0.345442 | 0.449218 | 0.844258 | 0.813042 | 0.843841 |
| C | 0.284978 | 0.375138 | 0.872532 | 0.846041 | 0.873083 |
| \|A-C\| | 0.080205 | 0.108518 | 0.031437 | 0.030945 | 0.028374 |
| \|A′-C\| | ***0.001164*** | ***0.003415*** | ***0.000738*** | ***0.000636*** | ***0.000704*** |
| \|B-C\| | 0.068235 | 0.088976 | 0.022937 | 0.022441 | 0.02246 |
| \|B′-C\| | ***0.060464*** | ***0.07408*** | 0.028274 | 0.032999 | 0.029242 |
| Data | $M_{G\_IDM\_135}$ | $M_{G\_COR\_0}$ | $M_{G\_COR\_45}$ | $M_{G\_COR\_90}$ | $M_{G\_COR\_135}$ |
| A | 0.875421 | 0.8768 | 0.838248 | 0.873746 | 0.835385 |
| B | 0.866655 | 0.857924 | 0.815655 | 0.858338 | 0.812924 |
| A′ | 0.844927 | 0.771295 | 0.705766 | 0.778357 | 0.706701 |
| B′ | 0.812289 | 0.745072 | 0.67549 | 0.750023 | 0.67471 |
| C | 0.846527 | 0.776141 | 0.710589 | 0.781922 | 0.712837 |
| \|A-C\| | 0.028894 | 0.100659 | 0.127659 | 0.091824 | 0.122548 |
| \|A′-C\| | ***0.0016*** | ***0.004846*** | ***0.004823*** | ***0.003565*** | ***0.006136*** |
| \|B-C\| | 0.020128 | 0.081783 | 0.105066 | 0.076416 | 0.100087 |
| \|B′-C\| | 0.034238 | ***0.031069*** | ***0.035099*** | ***0.031899*** | ***0.038127*** |
| Data | $M_{CCR\_0}$ | $M_{CCR\_1}$ | $M_{HSD}$ | - | - |
| A | 0.606402 | 0.393598 | 53 | - | - |
| B | 0.620295 | 0.379705 | 25 | - | - |
| A′ | 0.609028 | 0.390972 | 30 | - | - |
| B′ | 0.613897 | 0.386103 | 20 | - | - |
| C | 0.630838 | 0.369162 | 21 | - | - |
| \|A-C\| | 0.024436 | 0.024436 | 32 | - | - |
| \|A′-C\| | ***0.02181*** | ***0.02181*** | ***9*** | - | - |
| \|B-C\| | 0.010543 | 0.010543 | 4 | - | - |
| \|B′-C\| | 0.016941 | 0.016941 | ***1*** | - | - |

effect of lighting compensation method. Table 7 shows the results. A best and a worst results are shown here. In Table 7, the image data A and B show the same workpiece captured

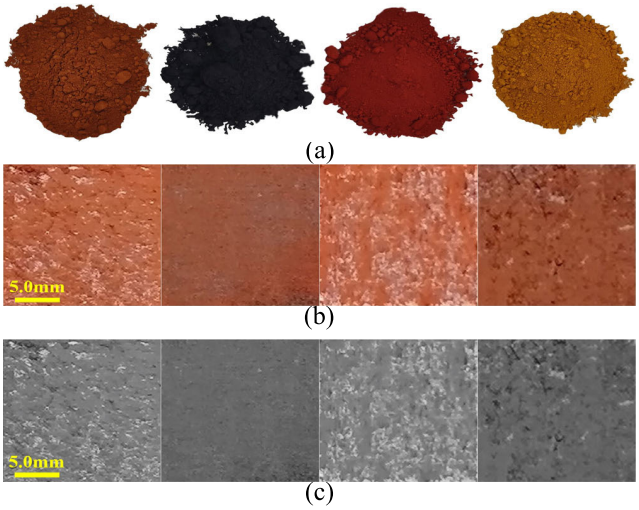


**FIGURE 10.** The photos of the oxide ponders and their typical corrosion mixtures: (a) is the photos of the typical iron oxides; (b) presents the examples of the typical oxide mixtures of (a); and (c) illustrates the gray image of (b).

under different environment light conditions. Data A′ and B′ are the lighting compensation results of A and B, respectively. And C is the standard imaging result of that workpiece whose environment light is best. Then we compute the feature offsets between the imaging results of A and C, A′ and C, B and C, and B′ and C. The values of |A-C| and |A′ -C|, and the results of |B-C| and |B′ -C| are compared. The smaller ones in |A′ -C| and |B′ -C| are marked by bold italics. After the light compensation, among 23 features, the dataset A′ can get 22 smaller offsets than A; and the dataset B′ can get 13 smaller results than B. The dataset B′ is the worst compensation effect in our experiment. Clearly, even the processing effect of dataset B′ is limited, it still can improve the computational stability than dataset B (i.e. 13>10). That can indicate the effectiveness of our method to some extent.

### C. EVALUATION OF CLEANING EFFECT CONTROL

A series of image features are computed to evaluate the corrosion state and control the laser output. The first feature vector is the GLCM texture vector. The angular second moment, the entropy, the contrast, the inverse differential moment, and the correlation are computed. These features can reflect the uniformity, the chaos degree, the depth, the regulation degree, and the orientation consistency of image texture, respectively. The second image feature vector is the concavo-convex region vector. It can assess the distribution state of the spot with small size or the pixel clump with big size in metal surface. In this paper, regarding the equations (4) and (6), $T_0 = T_1 = 125$. The third image feature is the histogram symmetry difference. It can distinguish the texture granularity degree before and after cleaning. Some computational results of these features are shown in Table 11. Regarding equation (7), the 3-order polynomial function is utilized to find the edge points of the histogram.

The imaging thermophysical property features include the typical corrosion gray intensity and the maximum cleaning temperature. When estimating the gray intensity, the analysis

**TABLE 8. The definitions of the typical corrosion type, the typical corrosion component and content, and the typical image gray distribution.**

| Typical corrosion type | Typical corrosion component & content | Imaging gray distribution |
|---|---|---|
| $TD_A$ | $\alpha$-$Fe_2O_3$ (48.7%), $\alpha$-FeOOH (31.8%), $Fe_3O_4$ (19.5%) | [123-144] |
| $TD_B$ | $\alpha$-$Fe_2O_3$ (61.2%), $\alpha$-FeOOH (24.3%), $Fe_3O_4$ (14.5%) | [96-123] |
| $TD_C$ | $\alpha$-$Fe_2O_3$ (70.3%), $\alpha$-FeOOH (18.8%), $Fe_3O_4$ (10.9%) | [144-255] |
| $TD_D$ | $\alpha$-$Fe_2O_3$ (39.6%), $\alpha$-FeOOH (38.2%), $Fe_3O_4$ (22.2%) | [0-96] |

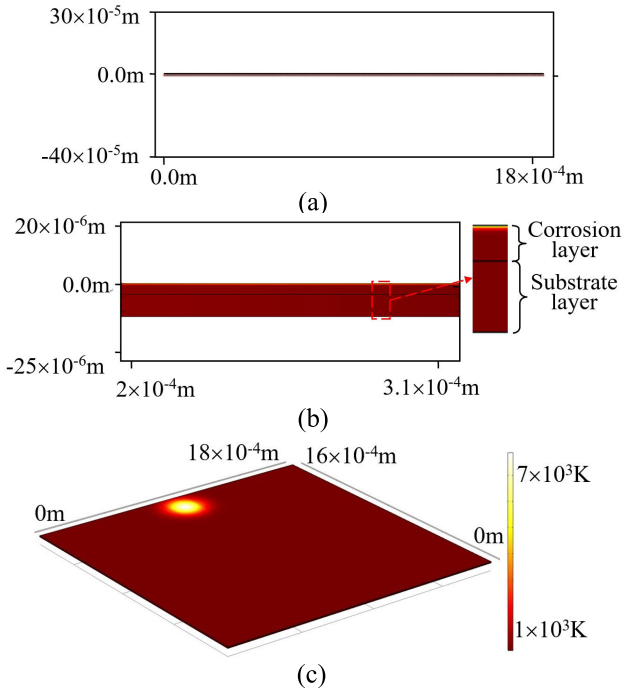


**FIGURE 11. The simulation interface samples of the maximum cleaning temperature estimation: (a) shows the 2D model of the corrosion layer and the carbon steel substrate; (b) is an amplification image of (a); and (c) presents the 3D sketch map of the laser cleaning process.**

results of Raman spectrum and some practical iron oxides are utilized. The Raman spectrum can analyze the typical corrosion component and content. And the iron oxides are used to create the typical oxide mixtures. Fig. 10 shows the powders of typical iron oxide and their mixtures. In Fig. 10, (a) is the photos of the typical iron oxides, they are $\alpha$-FeOOH, $Fe_3O_4$, $\alpha$-$Fe_2O_3$(deep brown), and $\alpha$-$Fe_2O_3$(brown); (b) shows the examples of typical oxide mixtures of (a) which are scattered in a polished carbon steel substrate; (c) is the gray image of (b). Table 8 presents the definitions of the typical corrosion type, the typical corrosion component and content, and the typical image gray distribution (see equation (9)). The gray distribution results come from the statistic calculations of the typical corrosion images.

To estimate the maximum temperature of laser cleaning, the COMSOL software [37] is utilized. Table 9 presents its main simulation parameters. From Table 9, only the laser power, the laser linear velocity, and the laser line space can

**TABLE 9. The simulation parameters of COMSOL software.**

| Laser beam radius (μm) | Single pulse energy (mJ) | Laser pulse width (ns) | Laser frequency (kHz) |
|---|---|---|---|
| 154.9045 | 5.99 | 60 | 20 |
| **Corrosion layer length (μm)** | **Corrosion layer thickness (μm)** | **Substrate layer length (μm)** | **Substrate layer thickness (μm)** |
| 1858.854 | 4.0 | 1858.854 | 8.0 |
| **Laser focal length (mm)** | **Laser absorptivity of corrosive layer** | **Initial temperature (K)** | **Laser power (W)** |
| 222.0 | 0.7 | 293.15 | 10-180 |
| **Laser linear velocity (mm/s)** | **Laser line space (mm)** | - | - |
| 500-6000 | 0.02-0.3 | - | - |

**TABLE 10. The thermophysical property parameters of typical corrosion components.**

| Investigated materials | | The thermophysical property parameters: Heat capacity at constant pressure (J/(kg·K)) | Heat transfer coefficient (W/(m·K)) | Material density ($kg/m^3$) |
|---|---|---|---|---|
| Typical corrosion component | $TD_A$ | 936.847 | 4.3 | 4104.2 |
| | $TD_B$ | 856.712 | 4.3 | 4104.2 |
| | $TD_C$ | 1150.591 | 4.3 | 4267.1 |
| | $TD_D$ | 1175.5 | 4.3 | 3806.2 |
| Carbon steel | | 502.0 | 44.5 | 7850.5 |

be tuned, while other parameters are set by the constants. Table 10 shows the corresponding measurement results of the thermophysical property parameters of the typical corrosion components in Table 8. Fig. 11 presents the main simulation results: (a) is the 2D model of the corrosion layer and the carbon steel substrate; (b) is an amplification image of (a); and (c) is the 3D sketch map of the laser cleaning process. Some assumptions are used in this simulation. First, the laser energy distribution fulfills the Gaussian type. Second, only the laser thermal effect is considered when carrying out our simulation. That means the thermal absorption effect of metal is neglected. Third, the boundary condition of thermal insulation is adopted for the thermal convection. Fourth, the thermal radiation during laser cleaning uses the Stephen-Boltzmann model [26]; and its thermal radiation rate of material is set by 0.68.

Some laser process parameters can be tuned in our proposed system. From Table 5 it can be seen that the laser has 7 process parameters; however, the practical situation is only few of them will be tuned. This is because: on one hand, most of the commercial lasers do not open their laser control interfaces; on the other hand, the laser service life and its working stability will become low if too many process parameters are tuned simultaneously during the cleaning. As a result, only three process parameters, i.e., the power, the linear velocity, and the line space, are tuned dynamically. Other parameters are set by some constants. For example, the laser frequency is set by 20kHz and the pulse width

**TABLE 11.** The data samples of image features, imaging thermophysical property features, and laser process parameters.

| Num | $M_{G\_ASM\_0}$ | $M_{G\_ASM\_45}$ | $M_{G\_ASM\_90}$ | $M_{G\_ASM\_135}$ | $M_{G\_ENT\_0}$ |
|---|---|---|---|---|---|
| 1 | 0.04678 | 0.03529 | 0.04079 | 0.03407 | 3.32377 |
| 2 | 0.04687 | 0.03574 | 0.04174 | 0.03431 | 3.30286 |
| 3 | 0.04066 | 0.02994 | 0.03595 | 0.03036 | 3.42885 |
| 4 | 0.04719 | 0.03449 | 0.04124 | 0.03503 | 3.2901 |
| 5 | 0.0467 | 0.03512 | 0.04176 | 0.03479 | 3.34021 |
| Num | $M_{G\_ENT\_45}$ | $M_{G\_ENT\_90}$ | $M_{G\_ENT\_135}$ | $M_{G\_CON\_0}$ | $M_{G\_CON\_45}$ |
| 1 | 3.60702 | 3.46803 | 3.63327 | 0.99394 | 1.93894 |
| 2 | 3.56934 | 3.42159 | 3.60459 | 0.94103 | 1.81041 |
| 3 | 3.72465 | 3.55467 | 3.70368 | 1.26737 | 2.58178 |
| 4 | 3.58902 | 3.41412 | 3.57171 | 0.92238 | 1.83101 |
| 5 | 3.60937 | 3.45933 | 3.62726 | 1.07203 | 2.05586 |
| Num | $M_{G\_CON\_90}$ | $M_{G\_CON\_135}$ | $M_{G\_IDM\_0}$ | $M_{G\_IDM\_45}$ | $M_{G\_IDM\_90}$ |
| 1 | 1.40443 | 2.09278 | 0.70944 | 0.61145 | 0.66049 |
| 2 | 1.26154 | 1.91929 | 0.71614 | 0.61337 | 0.67371 |
| 3 | 1.70233 | 2.43503 | 0.66964 | 0.56885 | 0.62471 |
| 4 | 1.19627 | 1.76047 | 0.72274 | 0.61186 | 0.67741 |
| 5 | 1.45338 | 2.16592 | 0.70039 | 0.59988 | 0.65946 |
| Num | $M_{G\_IDM\_135}$ | $M_{G\_COR\_0}$ | $M_{G\_COR\_45}$ | $M_{G\_COR\_90}$ | $M_{G\_COR\_135}$ |
| 1 | 0.59596 | 0.90538 | 0.81498 | 0.86663 | 0.8007 |
| 2 | 0.60464 | 0.91053 | 0.82824 | 0.88037 | 0.8178 |
| 3 | 0.56398 | 0.87641 | 0.74866 | 0.83448 | 0.76289 |
| 4 | 0.61509 | 0.91103 | 0.8241 | 0.88553 | 0.83094 |
| 5 | 0.5926 | 0.89964 | 0.80821 | 0.86412 | 0.79758 |
| Num | $M_{CCR\_0}$ | $M_{CCR\_1}$ | $M_{HSD}$ | $M_{ITP\_GI}$ | $M_{ITP\_TEM}$ |
| 1 | 0.51883 | 0.48118 | 65 | 3 | 2271.837 |
| 2 | 0.51125 | 0.48875 | 31 | 2 | 2880.351 |
| 3 | 0.53421 | 0.46579 | 36 | 1 | 4743.941 |
| 4 | 0.50804 | 0.49197 | 21 | 3 | 3586.573 |
| 5 | 0.50964 | 0.49036 | 46 | 4 | 4343.574 |
| Num | $M_{LPP\_LV}$ | $M_{LPP\_P}$ | $M_{LPP\_LS}$ | - | - |
| 1 | 1000 | 60 | 0.05 | - | - |
| 2 | 1000 | 80 | 0.05 | - | - |
| 3 | 500 | 120 | 0.075 | - | - |
| 4 | 1500 | 120 | 0.075 | - | - |
| 5 | 1000 | 140 | 0.05 | - | - |

**TABLE 12.** The selection methods of SVM supervising data.

| Cleaning effect degree | Cleaning effect description | SR distribution |
|---|---|---|
| 1 | The machined trace is almost invisible | [1.0, 2.0] |
| 2 | The machined trace is visible occasionally | [2.0, 2.6] |
| 3 | The machined trace is visible | [2.6, 5.2] |

is 60ns, etc. Finally, the input data samples of SVM can be presented in Table 11. They include the image features, the imaging thermophysical property features, and the laser parameters. In Table 11, the original input data are shown. The data normalization should be performed before the SVM training.

After the computation of the input data, the supervising data of SVM can be defined. In this paper, the supervising data use the cleaning effect, i.e., the analysis results of SR after cleaning, to carry out the SVM training. The SR is measured by a ZYGO NewView white-light interferometer. Its resolution in the horizontal direction is $0.36\mu$m$\sim$$9.5\mu$m; and the resolution in the vertical direction is about 0.1nm. Table 12 presents the corresponding distributions and descriptions of SR. In Table 12, we can classify the cleaning effect into 3 degrees, i.e., the SVM supervising data can be set by 1, 2, and 3. From Table 12 it also can be seen that the SR distribution of our application is comparable small. This is mainly because the carbon steel substrate has that similar SR distribution. In engineering, there are 14 or 15 degrees in SR grading [38]. Their specific scopes can distribute from 0.012 to 100. When evaluating the classification effect, the threshold $T_O^{SVM}$ in equation (12) is set by 0.1 in this paper.

**TABLE 13.** The experiment result comparisons using different training data combination modes.

| Num | Training feature vector | Classification precision |
|---|---|---|
| 1 | $[M_{GLCM}, M_{LPP}]$ | ≈66.667% |
| 2 | $[M_{CCR}, M_{LPP}]$ | ≈63.333% |
| 3 | $[M_{HSD}, M_{LPP}]$ | ≈50.0% |
| 4 | $[M_{ITP}, M_{LPP}]$ | ≈66.667% |
| 5 | $[M_{GLCM}, M_{CCR}, M_{LPP}]$ | ≈63.333% |
| 6 | $[M_{GLCM}, M_{HSD}, M_{LPP}]$ | ≈66.667% |
| 7 | $[M_{GLCM}, M_{ITP}, M_{LPP}]$ | ≈66.667% |
| 8 | $[M_{CCR}, M_{HSD}, M_{LPP}]$ | ≈73.333% |
| 9 | $[M_{CCR}, M_{ITP}, M_{LPP}]$ | ≈66.667% |
| 10 | $[M_{ITP}, M_{HSD}, M_{LPP}]$ | ≈76.667% |
| 11 | $[M_{GLCM}, M_{CCR}, M_{HSD}, M_{LPP}]$ | ≈80.0% |
| 12 | $[M_{GLCM}, M_{CCR}, M_{ITP}, M_{LPP}]$ | ≈80.0% |
| 13 | $[M_{GLCM}, M_{HSD}, M_{ITP}, M_{LPP}]$ | ≈70.0% |
| 14 | $[M_{CCR}, M_{HSD}, M_{TIP}, M_{LPP}]$ | ≈83.33% |
| **15** | $\boldsymbol{[M_{GLCM}, M_{CCR}, M_{HSD}, M_{ITP}, M_{LPP}]}$ | **≈90.0%** |

To assess the computation effect of SVM, a series of comparison experiments are performed. Table 13 shows the comparison results of SVM classification precision using different feature combinations. In Table 13, we almost traverse all the possible combination modes of the features presented in Table 1. The features or the feature combinations which are not illustrated in Table 13 indicate that their classification accuracies are too low. The training data amount in Table 13 is 300 and the test data amount is 30. From Table 13, our proposed feature combination mode can achieve the best classification precision. The corresponding result is illustrated in bold. Some other image features are also tested in this experiment including the Gabor wavelet features [39], the LBP features, and other GLCM texture features [40], etc.; however, the practical experiment results show their poor performances. For example, the classification precisions of them are always lower than 60%.

Some other machine learning methods [41] are also tested. For example, the prediction accuracy of the neural network [42] cannot be large than 60% in our experiment. This is because the training data amount is limited currently. In our past research works [43], the SVM has been successfully applied in designing the multiple-input and single-output prediction model. A Monte Carlo and SVM iteration algorithm [28] has also been developed. Thus the SVM is considered in this paper. To test the performance of SVM further, a comparison experiment is implemented: different kernel functions are used to evaluate the prediction effect of SVM. The data amounts of the training data and the test data are 300 and 30, respectively. And after the test it can be found that the prediction accuracies of the linear kernel function,

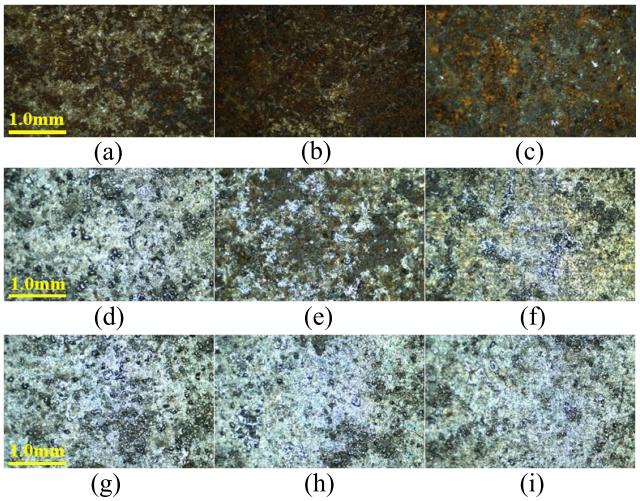


**FIGURE 12.** The comparisons of cleaning result photos using the traditional cleaning process and our proposed method: (a) to (c) are the original corrosion metal images; (d) to (f) present the cleaning results using the traditional method; and (g) to (i) show the results of our method.

the polynomial kernel function, the radial basis kernel function, and the sigmoid kernel function of SVM are 56.7%, 90.0%, 43.3%, and 26.7%, respectively. Lastly, the polynomial kernel function is selected for the SVM.

An iteration computation is used to find the proper laser parameters. Fig. 12 shows the corrosion images and the cleaning results which use the traditional process and our method. The traditional process uses the artificial experience to build the cleaning regulation: if its processing effect can fulfill most of the user's demands, it will become a standard for the industrial department. The laser parameters of the traditional method in this experiment are: the linear velocity is 1000mm/s, the power is 120W, and the line space is 0.05mm. In Fig. 11, (a) to (c) are the corrosion metal images; (d) to (f) are the cleaning results of traditional method; and (g) to (i) are the results of our method. The measured SR are 2.452, 1.987, 2.246, 2.508, 2.318, and 2.138 from (d) to (i), respectively. Because the corrosion degrees are different, the cleaning effects will vary a lot if the changeless laser parameters are used. Clearly, the results of our method can position SR in the same SR degree (see Table 7); while the result of the traditional method cannot achieve it.

### D. EVALUATION OF SR PRIDICTION

After the cleaning effect prediction and the laser cleaning, the specific value of SR can be forecasted by the new captured images. Fig. 13 shows some image samples after cleaning. In Fig. 13, the data in (a), (b) and (c) are the images with the SR degrees 1, 2, and 3, respectively. From Fig. 13, it can be seen that the image features of different SR degrees are apparent: the metal texture information become clearer from (a) to (c); and the laser motion trace can even be observed in (c). From Fig. 13 it can be deduced that more corrosion components exist in (a); after the exfoliation of corrosion layer, more original metal textures can be exposed in (b); and a comparable serious laser ablation happens in (c). From these results above, it can be concluded that: comparing with the image data in Fig. 8 (d) which are covered by the corrosion layers, it is possible to use the classification degree of laser cleaning effect and the corresponding image features of the cleaned metal to predict the SR precisely.

**TABLE 14.** The computation results of image feature for SR prediction under different cleaning effects.

| Num | $M_{T\_coa}{}^{a}$ | $M_{CCR\_1}{}^{a}$ | $M_{CCR\_1}{}^{b}$ | $M_{G\_COR}{}^{AVEb}$ | $M_{G\_COR}{}^{AVEc}$ |
|---|---|---|---|---|---|
| 1 | 1.91958 | 0.524624 | 0.261468 | 0.819097 | 0.8443 |
| 2 | 1.91395 | 0.47568 | 0.268232 | 0.802568 | 0.87707 |
| 3 | 1.90491 | 0.470968 | 0.173988 | 0.768005 | 0.81379 |
| 4 | 1.905636 | 0.42412 | 0.238248 | 0.830688 | 0.85074 |
| 5 | 1.878269 | 0.38802 | 0.406976 | 0.800627 | 0.87445 |

[a] The cleaning effect degree 1. [b] The cleaning effect degree 2. [c] The cleaning effect degree 3.

A series of image features are computed for the SR prediction. Table 14 shows the computational samples of them. The features in Table 14 give out the best features for SR prediction in our experiment. Regarding the images under the SR degree 1, because the existence of the metal corrosion layer, the thin texture and the small corrosive spot can be observed here and there in the metal surface; as a result, the Tamura coarseness and the convex region feature can be used to represent these image features. As for the images under the SR degree 2, the irregular textures can be observed. Parts of them come from the corrosion component and parts of them belong to the metal texture. Thus both the convex region feature and the GLCM correlation feature are considered to compute these thin and coarse textures. And when it comes to the images under the SR degree 3, the coarse textures can be observed; and these textures also have the apparent orientation consistency; therefore the GLCM correlation are calculated again. In Table 14, the original feature data are illustrated.

A series of comparison experiments are implemented to assess the prediction effect of proposed method. Table 15 shows the corresponding results. Many features and feature combination modes are employed to test the prediction accuracy of SR. The GLCM features, the Tamura texture feature, the Gabor wavelet features, and the LBP features are all considered here. After the experimental tests, the best combination results are illustrated in Table 15. In Table 15, if the SR offset between the actual value and the forested value is less than 0.1, it is thought the predicted result is correct. From Table 15 it can be seen that different feature combination modes are used for the image data with different cleaning effects. The SVR, the n-order polynomial function, and the linear regression method are all utilized to perform the SR forecasting computation. Regarding the SVR, the amount of training data is 100, and the amount of test data is 30. As for the n-order polynomial function and the linear regression function, the amounts of fitting data are both 30.

### E. THE PRACTICAL APPLICATION ISSUE OF PROPOSED SYSTEM AND METHOD

In this paper, an iteration computation is utilized to find the proper laser process parameters. The SVM is in charge

**TABLE 15. The prediction accuracy comparisons of SR using different image features and feature combinations.**

| Cleaning effect degree | Image feature | Prediction method | Prediction accuracy |
|---|---|---|---|
| 1 | [$M_{GLCM}$, $M_{T\_Coa}$, $M_{CCR\_I}$] | SVR | ≈76.7% |
| 1 | [$M_{G\_COR}{}^{AVE}$] | Linear function | ≈80.0% |
| 1 | [$M_{G\_ASM}{}^{AVE}$] | 2-order polynomial function | ≈83.3% |
| **1** | **[$M_{T\_Coa}$]** | **Linear function** | **≈86.7%** |
| **1** | **[$M_{CCR\_I}$]** | **3-order polynomial function** | **≈86.7%** |
| 2 | [$M_{G\_ASM}{}^{AVE}$] | 2-order polynomial function | ≈70.0% |
| 2 | [$M_{T\_Coa}$] | 2-order polynomial function | ≈73.3% |
| 2 | [$M_{CCR\_I}$, $M_{T\_Coa}$] | SVR | ≈73.3% |
| **2** | **[$M_{CCR\_I}$]** | **3-order polynomial function** | **≈83.3%** |
| **2** | **[$M_{G\_COR}{}^{AVE}$]** | **3-order polynomial function** | **≈83.3%** |
| 3 | [$M_{G\_ASM}{}^{AVE}$] | 2-order polynomial function | ≈70.0% |
| 3 | [$M_{G\_ENT}{}^{AVE}$] | 2-order polynomial function | ≈70.0% |
| 3 | [$M_{G\_COR}{}^{AVE}$] | Line function | ≈70.0% |
| 3 | [$M_{T\_Coa}$] | 3-order polynomial function | ≈80.0% |
| **3** | **[$M_{G\_COR}{}^{AVE}$]** | **3-order polynomial function** | **≈83.3%** |

with the cleaning effect classification. The random number generation method is employed to create the laser process parameter candidates for SVM. In the practical terms, the random number is not a real random number; in fact we build a table of the typical laser process parameters for the marine corrosion metal cleaning. In this table, the selected values of the laser process parameter are not continuous. In the practical computation, we only need to select the corresponding process data randomly from this table and implement the SVM prediction. If the SVM fails to forecast a proper laser process parameters after traversing all the data in this table, the user has to use his or her own experience to tune the laser parameters. And if the cleaning effect can fulfill the request of user, then the corresponding experience data will be added and saved into that table.

In Tables 1 and 2, almost all the features can be computed from image directly, only the features $M_{HSD}$ and $M_{ITP\_TEM}$ are the exceptions. Regarding $M_{HSD}$, because we cannot get the real histogram after cleaning, lots of typical histograms after cleaning are saved in our system in advance. When carrying out the practical computation, we use the result of $M_{ITP\_GI}$ to judge the typical corrosion type firstly, and then call the typical histogram above according to its corresponding laser process parameters. As for $M_{ITP\_TEM}$, it is also not realistic to use COMSOL to estimate its maximum cleaning temperature online. Like the solution above the similar measurement is utilized. To evaluate the proposed method further, both the laser parameters tuning and the SR prediction are performed. If the user defines his or her expected SR output scope as [$SR_1$, $SR_2$] ($|SR_2\text{-}SR_1| \leq 0.2$), we can use the middle value of this scope to set the expected output of SVM. Its computation method is shown in (19). After some tests, the final control and prediction accuracy of SR can approach 80.0%.

$$O_{SVM}^{user} = (SR_1 + SR_2)/2 \tag{19}$$

where $SR_1$ and $SR_2$ are the boundaries of the user expected SR output.

### F. DISCUSSIONS

A new laser cleaning process for the marine corrosion metal is investigated in this paper. The marine corrosion belongs to a kind of electrochemical corrosion. Generally speaking, the corrosion creation experiences a complex process. In its early stage, the corrosion mainly is the pitting corrosion. The corresponding components include $\alpha$-$Fe_2O_3$ and $\gamma$-FeOOH, etc. Their colors are faint yellow and tan. In the second stage, the corrosion becomes the rust spots, the multi-layer corrosion appears. The corrosion components in the surface layer are $\alpha$-FeOOH or $\gamma$-FeOOH, etc.; while the corrosions in the inner layer include $\alpha$-$Fe_2O_3$ and $Fe_3O_4$, etc. The color of corrosion layer is redish brown or brown. In the third stage, the corrosion becomes a thick layer. Its components include $\alpha$-FeOOH and $Fe_3O_4$, etc. Their colors include black and dark brown. In this paper we mainly consider the corrosion issue of the second stage. That is because if the corrosion layer is too thick the carbon steel will be replaced directly and no laser cleaning is needed.

The SR estimation is necessary when implementing the ship maintenance task. In the past, the laser cleaning-based maintenance flows are: first lots of laser cleaning experiments will be performed to get the experience values of process parameters. Second, a process standard will be built. Once this standard is made, the laser parameters will not be changed any more during the whole cleaning process. Third, when carrying out the laser cleaning, the workers will judge the metal corrosion state and perform the cleaning operation according to their individual experiences and the guidance of process regulation. Fourth, the SR will be measured after cleaning. If the SR is not qualified, the further processing will be performed. Clearly, the operation processes above are passive: we only can assess SR after the surface processing. If the SR after laser cleaning can be controlled and estimated before and during the cleaning, that will be real meaningful for the practical ship maintenance.

The artificial intelligence technique can be used to improve the automatic level of our system. Recently, there are some similar intelligent methods [44] which have been proposed for the laser precision machining applications. In [45], the artificial neural network was utilized to predict the process parameters of laser cutting. In [46], the deep neural networks and the reinforcement learning were considered to improve the intelligence degree of laser welding. After the extensive studies of the similar technique, it can be found the intelligence technique is not widely used for the laser-related application currently for two reasons. On one hand, the diversity

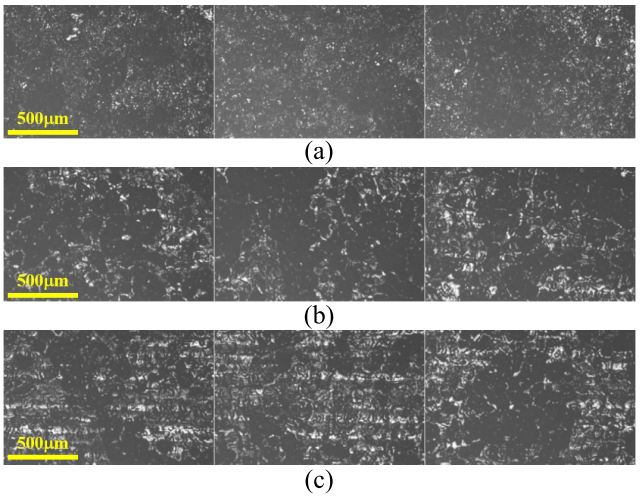


**FIGURE 13.** The image data samples after laser cleaning: (a) shows the images with the SR degree 1; (b) presents the photos with the SR degree 2; and (c) illustrates the results with the SR degree 3.

of the practical working condition and the huge requirement of the training data limit the application scopes of most of the intelligence methods. On the other hand, the constant tuning of laser parameters during cleaning will also decrease the lifetime and the stability of laser. Thus after the researches of the image features [47] and the laser cleaning effect [48], a two-stage algorithm is developed.

Lots of imaging features are utilized in this paper. Except for the GLCM texture features, other imaging features are the new developed ones. First, the concavo-convex region features are proposed. These features can describe the texture spot information in the metal surface. Second, a feature of histogram symmetry difference is defined. It can measure the ratio difference between the metal texture and the corrosion texture. Third, the imaging thermophysical property features are also designed. They can represent the gray intensity distribution of typical corrosion component and the corresponding maximum cleaning temperature. Clearly, the maximum cleaning temperature is related with the analysis result of the imaging gray distribution of typical corrosion. Hence it can be looked on as a kind of special imaging feature. Many other image features, such as the LBP features or the Gabor wavelet coefficients etc., are also tested; however they are not considered in the practical application for their poor performances.

When estimating the imaging intensity feature $M_{ITP\_GI}$ of the typical corrosion, the Raman spectrum is used to determine its main components and contents. To get the analysis results of Raman spectrum, the Gaussian distribution function is used to estimate the area of Raman peak after the baseline correction [49]. Then the peak area can be regarded as an important reference for the typical corrosion content estimation. Fig. 14 shows the example of the baseline correction and the peak fitting of Raman spectrum before cleaning. In Fig. 14, (a) is a sample of the original Raman spectrum and its result of baseline correction; (b) is the result of Raman peak fitting. Table 16 shows the component and the

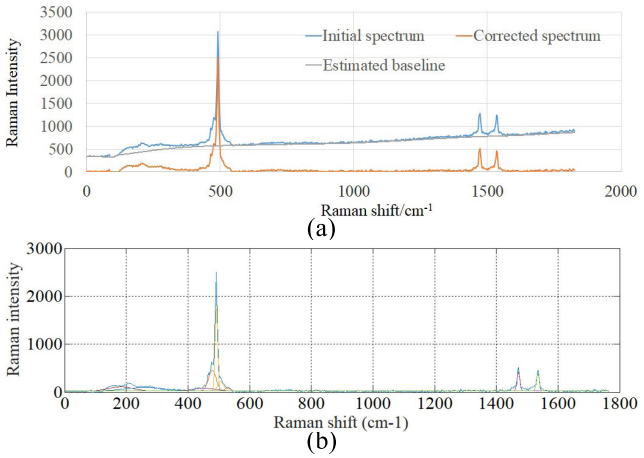


**FIGURE 14.** The example of Raman spectrum data processing: (a) is the sample of the original Raman spectrum and its result of the baseline correction; (b) presents the result of Raman peak fitting.

**TABLE 16.** The example of corrosion component, Raman shift, and Raman peak area.

| Corrosion component | Raman shift ($cm^{-1}$) / peak area |
|---|---|
| α-$Fe_2O_3$ | 259/11301.5, 479/13368.75 |
| $Fe_3O_4$ | 506/4682.872, 528/1305.305 |
| α-FeOOH | 452/5359.995 |
| γ-$Fe_2O_3$ | 708/1335.78 |
| γ-FeOOH | 1312/741.541 |

content analysis results of Fig. 14. Clearly, comparing with the final component ratio which is illustrated in Table 8, the results in Table 16 are more complex. To decrease the analysis complexity, and we also consider that the colors of some iron oxides are similar, lastly only the content ratios in Table 8 are used. The computational effect of SVM has proofed its effectiveness.

In this paper we partition one big workpiece into several small rectangle blocks; and in each block the particular laser cleaning will be carried out. Since the laser parameters are unchanged during the cleaning of each small block, there is no processing time limitation for our algorithm because the corresponding computation has been finished before cleaning. A kind of SVM-based iteration computation is proposed to find the proper laser parameters. The inputs of SVM include the random numbers of laser parameters and the imaging features. As we have stated, the laser parameters are not the real random numbers. They are selected from a predefined table. Comparing with other optimization methods [50], [51] which can estimate the optimal results by updating their computational strategies dynamically, our algorithm just selects and tests the known parameters from a table. Strictly speaking, our algorithm does not belong to a traditional optimal computation [52], [53]. Then it is not necessary to consider its convergence or efficiency.

When implementing our cleaning technique for the workpiece with big size, the overlapping issue should also be considered. The overlapping issue is to solve the laser cleaning process regarding the neighboring cleaning blocks (see Fig. 2 (b)). Fig. 15 shows the sketch maps and the actual

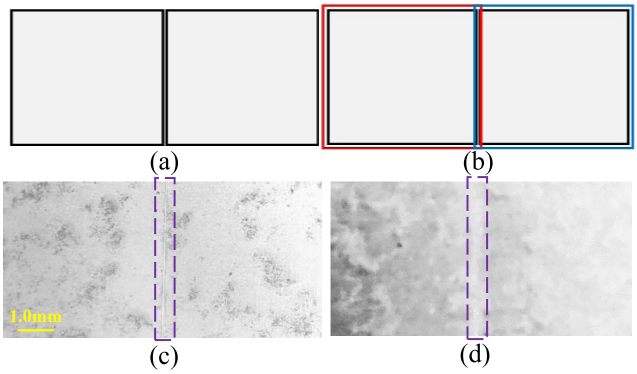


**FIGURE 15.** The sketch maps and the actual images of the overlapping process issue: (a) and (b) are the sketch maps of the overlapping problem; (c) and (d) show the actual processing results.

applications of that issue. In Fig. 15, (a) and (b) are the sketch maps of the overlapping problem; (c) and (d) are the actual processing results of them. During the practical cleaning process, a linear gap may appear between the neighboring cleaning blocks (see Fig. 15 (a) and (c)) because of the positioning error of the Cartesian coordinate robot. To solve that problem, we enlarge the size of the original cleaning region to some extent (see the red and the blue rectangles in Fig. 15 (b)). For example, the 1.05 times of the original cleaning size can be considered in this paper. Clearly, the region of linear gap will be cleaned for more than one times. If the output of laser is set properly, the negative effect of the multi-times cleaning can be omitted.

The proposed method at least has three advantages. First, its intelligence degree [54] is high. Comparing with the traditional cleaning method, our method can control the laser output intelligently and predict the SR automatically. Second, its computation stability is good. The proposed method uses the image features and the imaging thermophysical property features to carry out the attribution analysis of the corrosion workpiece. With the assistances of both the environment lighting control and the Raman spectrum analysis, its processing effect is stable. Third, the accuracy of proposed method is also acceptable. According to the experimental analyses, the computational accuracies of SVM and 3-order polynomial function can be large than 90.0% and 80.0% in many cases, respectively; and the integrated processing accuracy of our system can also approach 80.0%. Clearly, our proposed method also has some shortcomings. For example, the processing speed of proposed method is comparable slow than the traditional technique. And its processing accuracy can be improved furtherly in future.

## V. CONCLUSION

To fulfill the surface processing demand of user, a kind of process parameters tuning and SR estimation algorithm for laser cleaning application is proposed. Before the implementation of cleaning, the proper laser parameters are estimated. A series of features, i.e. the GLCM features, the concavo-convex region features, the histogram feature, and the imaging thermophysical property features are computed. And a SVM-based iterative computation is employed. After the laser cleaning, the SR can be predicted. The image features, such as the Tamura coarseness, the GLCM features, and the convex feature are calculated for the image after cleaning. To improve the prediction precision, different feature combinations are used for images with different cleaning effect degrees. In future, more data will be accumulated and some intelligent computational methods can be designed to improve the processing effect of our system.

## REFERENCES

[1] B. Lukiyanchuk, *Laser Cleaning*. Singapore: World Scientific Publishing Company Press, 2002.

[2] V. Gomes, A. Dionísio, J. S. Pozo-Antonio, T. Rivas, and A. Ramil, "Mechanical and laser cleaning of spray graffiti paints on a granite subjected to a $SO_2$-rich atmosphere," *Construct. Building Mater.*, vol. 188, pp. 621–632, Nov. 2018.

[3] C. Feng, Y. Zhang, J. Liu, Y. Qian, J. Zhang, J. Zhao, F. Shi, and X. Bai, "Optimized chemical cleaning procedure for enhancing photoemission from GaAs photocathode," *Mater. Sci. Semicond. Process.*, vol. 91, pp. 41–46, Mar. 2019.

[4] W. Tangsopa and J. Thongsri, "Development of an industrial ultrasonic cleaning tank based on harmonic response analysis," *Ultrasonics*, vol. 91, pp. 68–76, Jan. 2019.

[5] D. Grojo, M. BoyoMo-Onana, A. Cros, and P. Delaporte, "Influence of laser pulse shape on dry laser cleaning," *Appl. Surf. Sci.*, vol. 252, no. 13, pp. 4786–4791, Apr. 2006.

[6] M. K. A. A. Razab, A. M. Noor, M. S. Jaafar, N. H. Abdullah, F. M. Suhaimi, M. Mohamed, N. Adam, and N. A. A. N. Yusuf, "A review of incorporating Nd: YAG laser cleaning principal in automotive industry," *J. Radiat. Res. Appl. Sci.*, vol. 11, no. 4, pp. 393–402, Oct. 2018.

[7] T. Shi, C. Wang, G. Mi, and F. Yan, "A study of microstructure and mechanical properties of aluminum alloy using laser cleaning," *J. Manuf. Process.*, vol. 42, pp. 60–66, Jun. 2019.

[8] K. He, M. Gao, and Z. Zhao, "Soft computing techniques for surface roughness prediction in hard turning: A literature review," *IEEE Access*, vol. 7, pp. 89556–89569, 2019.

[9] S. K. Chakrapani, A. Howard, and D. Barnard, "Influence of surface roughness on the measurement of acoustic nonlinearity parameter of solids using contact piezoelectric transducers," *Ultrasonics*, vol. 84, pp. 112–118, Mar. 2018.

[10] V. V. Alexander, H. Deng, M. N. Islam, and F. L. Terry, "Non-contact surface roughness measurement of crankshaft journal using a supercontinuum laser," in *Proc. CLEO/QELS, LSPA*, San Jose, CA, USA, May 2010, pp. 16–21, Paper AFA3.

[11] T. Hatakeyama, R. Kibushi, M. Ishizuka, and T. Tomimura, "Fundamental study of surface roughness dependence of thermal and electrical contact resistance," in *Proc. ITHERM*, Las Vegas, NV, USA, May/Jun. 2016, pp. 1078–1082.

[12] M. Vidal, M. Ostra, N. Imaz, E. Garcia-Lecina, and C. Ubide, "Feature descriptions from scanned images of chromium electrodeposits as predictor parameters of surface roughness and crystallographic texture," *Chemometr. Intell. Lab.*, vol. 149, pp. 90–98, Dec. 2015.

[13] R. Elemuren, A. Tamsaki, R. Evitts, I. N. A. Oguocha, G. Kennell, R. Gerspacher, and A. Odeshi, "Erosion-corrosion of 90 AISI 1018 steel elbows in potash slurry: Effect of particle concentration on surface roughness," *Wear*, vols. 430–431, pp. 37–49, Jul. 2019.

[14] L. Zhou, H. Liu, X. Zhuang, and D. Liu, "Study on brittle graphite surface roughness detection based on gray-level co-occurrence matrix," in *Proc. ICMCCE*, Huhhot, China, Sep. 2018, pp. 273–276.

[15] S. Ghodrati, M. Mohseni, and S. G. Kandi, "Application of image edge detection methods for precise estimation of the standard surface roughness parameters: Polypropylene/ethylene-propylene-diene-monomer blend as a case study," *Measurement*, vol. 138, pp. 80–90, May 2019.

[16] J. Kim, H. Lim, S. C. Ahn, and S. Lee, "RGBD camera based material recognition via surface roughness estimation," in *Proc. IEEE-WAVC*, Lake Tahoe, NV, USA, Mar. 2018, pp. 1963–1971.

[17] N. A. Hameed, I. M. Ali, and H. K. Hassun, "Calculating surface roughness for a large scale SEM images by mean of image processing," *Energy Procedia*, vol. 157, pp. 84–89, Jan. 2019.

[18] R. Wang, H. Qu, Y. Sui, and J. Lv, "Calibration of Cartesian robot based on machine vision," in *Proc. IEEE-ITOEC*, Chongqing, China, Oct. 2017, pp. 1103–1108.
[19] M. Al-Qatf, Y. Lasheng, M. Al-Habib, and K. Al-Sabahi, "Deep learning approach combining sparse autoencoder with SVM for network intrusion detection," *IEEE Access*, vol. 6, pp. 52843–52856, 2018.
[20] J. Rong, Z. Kang, S. Chen, D. Yang, J. Huang, and J. Yang, "Growth kinetics and thickness prediction of interfacial intermetallic compounds between solid steel and molten aluminum based on thermophysical simulation in a few seconds," *Mater. Characterization*, vol. 132, pp. 413–421, Oct. 2017.
[21] F. Zhang, H. Liu, C. Suebka, Y. Liu, Z. Liu, W. Guo, Y. Cheng, S. Zhang, and L. Li, "Corrosion behavior of laser-cleaned AA7024 aluminum alloy," *Appl. Surf. Sci.*, vol. 435, pp. 452–461, Mar. 2018.
[22] M. Yang, J. Dai, L. Wang, Y. Li, and Y. Song, "First principles study of structural stability against the distribution of Mg and Al atoms and adsorption behaviors of heavy metals of attapulgite," *Comput. Mater. Sci.*, vol. 169, Nov. 2019, Art. no. 109106.
[23] P. Fathi, M. Rafieazad, X. Duan, M. Mohammadi, and A. M. Nasiri, "On microstructure and corrosion behaviour of AlSi10Mg alloy with low surface roughness fabricated by direct metal laser sintering," *Corrosion Sci.*, vol. 157, pp. 126–145, Aug. 2019.
[24] N. Gathimba, Y. Kitane, T. Yoshida, and Y. Itoh, "Surface roughness characteristics of corroded steel pipe piles exposed to marine environment," *Construct. Building Mater.*, vol. 203, pp. 267–281, Apr. 2019.
[25] J. Yuan, L. Liang, and G. Lin, "Study on processing characteristics and mechanisms of thermally assisted laser materials processing," *Surf. Coat. Technol.*, vol. 378, Nov. 2019, Art. no. 124946.
[26] J. Li, *Laser Diffraction and Thermal Effect Computation*. Beijing, China: Science Press, 2002.
[27] A. Campbell, P. Murray, E. Yakushina, S. Marshall, and W. Ion, "New methods for automatic quantification of microstructural features using digital image processing," *Mater. Des.*, vol. 141, pp. 395–406, Mar. 2018.
[28] H. Liu, D. Shi, X. Hou, B. Yan, and W. Wang, "Manufacture process quality control of interferometric fibre optic gyroscope using analyses of multi-type assembly and test data," *Int. J. Comput. Integr. Manuf.*, vol. 11, no. 31, pp. 1124–1140, Aug. 2018.
[29] H. Zhang, Z. Luo, Z. He, and K. Lu, "Tamura coarseness for evaluating OTH radar image and its application in RFI suppression," in *Proc. IEEE Radar*, Boston, MA, USA, Apr. 2019, pp. 1–6.
[30] Q. Fu, C. Jung, and K. Xu, "Retinex-based perceptual contrast enhancement in images using luminance adaption," *IEEE Access*, vol. 6, pp. 61277–61286, Oct. 2018.
[31] J. Chen, H. Liu, J. Zheng, M. Lv, B. Yan, X. Hu, and Y. Gao, "Damage degree evaluation of earthquake area using UAV aerial image," *Int. J. Aerosp. Eng.*, vol. 2016, Jun. 2016, Art. no. 2052603.
[32] A. K. Kadiyala, M. Sharma, and J. Bijwe, "Exploration of thermoplastic polyimide as high temperature adhesive and understanding the interfacial chemistry using XPS, ToF-SIMS and Raman spectroscopy," *Mater. Des.*, vol. 109, pp. 622–633, Nov. 2016.
[33] H.-S. Tran, J. Tchuindjang, H. Paydas, A. Mertens, R. Jardin, L. Duchêne, R. Carrus, J. Lecomte-Beckers, and A. Habraken, "3D thermal finite element analysis of laser cladding processed Ti-6Al-4V part with microstructural correlations," *Mater. Des.*, vol. 128, pp. 130–142, Aug. 2017.
[34] Q. Li, W. Li, and M. An, "Sunlight induced photoelectrochemical anticorrosion effect of corrosion product layers on electrogalvanized steel in simulated seawater," *Electrochem. Commun.*, vol. 90, pp. 39–42, May 2018.
[35] K. Firuzi, M. Vakilian, B. T. Phung, and T. R. Blackburn, "Partial discharges pattern recognition of transformer defect model by LBP & HOG features," *IEEE Trans. Power Del.*, vol. 34, no. 2, pp. 542–550, Apr. 2019.
[36] D. He, Y. Lin, J. Chen, D. Chen, J. Huang, Y. Tang, and M. Chen, "Microstructural evaluation and support vector regression model for an aged Ni-based superalloy during two-stage hot forming with stepped strain rates," *Mater. Des.*, vol. 164, pp. 51–62, Sep. 2018.
[37] A. Ying, H. Zhang, B. Merrill, M.-Y. Ahn, and S. Cho, "Breeding blanket system design implications on tritium transport and permeation with high tritium ion implantation: A MATLAB/simulink, COMSOL integrated dynamic tritium transport model for HCCR TBS," *Fusion Eng. Des.*, vol. 136, pp. 1153–1160, Nov. 2018.
[38] P. Liu, and Y. Zhang, *Foundation of Mechanical Precision Design and Testing*. Harbin, China: Harbin Institute of Technology Press, 2003.
[39] J. Ilonen, J.-K. Kamarainen, P. Paalanen, M. Hamouz, J. Kittler, and H. Kalviainen, "Image feature localization by multiple hypothesis testing of Gabor features," *IEEE Trans. Image Process.*, vol. 17, no. 3, pp. 311–325, Mar. 2008.
[40] M. Umaselvi, S. S. Kumar, and M. Athithya, "Color based urban and agricultural land classification by GLCM texture features," in *Proc. IET-SEISCON*, Tiruchengode, India, Dec. 2012, pp. 1–4.
[41] M. Odstrcil, A. Murari, and J. Mlynar, "Comparison of advanced machine learning tools for disruption prediction and disruption studies," *IEEE Trans. Plasma Sci.*, vol. 41, no. 7, pp. 1751–1759, Jul. 2013.
[42] S. S. Pouriyeh Vahid, G. Sannino, G. D. Pietro, H. Arabnia, and J. Gutierrez, "A comprehensive investigation and comparison of machine learning techniques in the domain of heart disease," in *Proc. ISCC*, Heraklion, Greece, Jul. 2017, pp. 204–207.
[43] H. Liu, Y. Ma, W. Wang, and B. Yan, "Non-destructive testing and assembly quality evaluation of IFOG optical path," *J. Optoelectron. Adv. Mater.*, vol. 21, nos. 3–4, pp. 171–179, Mar.-Apr. 2019.
[44] S. Ocylok, E. Alexeev, S. Mann, A. Weisheit, K. Wissenbach, and I. Kelbassa, "Correlations of melt pool geometry and process parameters during laser metal deposition by coaxial process monitoring," *Phys. Procedia*, vol. 56, pp. 228–238, Dec. 2014.
[45] J. Chen, R. Xiao, T. Zuo, and Y. Wang, "Intelligent system for selecting laser cutting parameters," *Chin. J. Laser.*, vol. 31, no. 6, pp. 757–760, Jun. 2004.
[46] J. Gunther, P. M. Pilarski, G. Helfrich, H. Shen, and K. Diepold, "Intelligent laser welding through representation, prediction, and control learning: An architecture with deep neural networks and reinforcement leaning," *Mechatronics*, vol. 34, pp. 1–11, Mar. 2016.
[47] H. Liu, H. Lu, and Y. Zhang, "Image enhancement for outdoor long-range surveillance using IQ-learning multiscale Retinex," *IET Image Process.*, vol. 11, no. 9, pp. 786–795, Sep. 2017.
[48] H. Liu, Y. Xue, J. Li, W. Wu, and J. Lan, "Investigation of laser power output and its effect on Raman spectrum for marine metal corrosion cleaning," *Energies*, vol. 13, no. 1, p. 12, Dec. 2019.
[49] Z. Sobhani, M. A. Amin, R. Naidu, M. Megharaj, and C. Fang, "Identification and visualisation of microplastics by Raman mapping," *Anal. Chim. Acta*, vol. 1077, pp. 191–199, Oct. 2019.
[50] R. P. Alvarez Gil, Z. C. Johanyak, and T. Kovacs, "Surrogate model based optimization of traffic lights cycles and green period ratios using microscopic simulation and fuzzy rule interpolation," *Int. J. Artif. Intell.*, vol. 16, no. 1, pp. 20–40, Mar. 2018.
[51] U. Kose and A. Arslan, "Optimization of self-learning in computer engineering courses: An intelligent software system supported by artificial neural network and vortex optimization algorithm," *Comput. Appl. Eng. Educ.*, vol. 25, no. 1, pp. 142–156, Jan. 2017.
[52] K. K. Sarma, "Neural network based feature extraction for assamese character and numeral recognition," *Int. J. Artif. Intell.*, vol. 2, no. S09, pp. 37–56, Jan. 2009.
[53] C. Pozna, R.-E. Precup, J. K. Tar, I. Škrjanc, and S. Preitl, "New results in modelling derived from Bayesian filtering," *Knowl.-Based Syst.*, vol. 23, no. 2, pp. 182–194, Mar. 2010.
[54] M. A. Hannan, J. A. Ali, P. J. Ker, A. Mohamed, M. S. H. Lipu, and A. Hussain, "Switching techniques and intelligent controllers for induction motor drive: Issues and recommendations," *IEEE Access*, vol. 6, pp. 47489–47510, 2018.

**HAOTING LIU** received the Ph.D. degree from the Institute of Automation, Chinese Academy of Sciences, in 2010. He is currently an Associate Professor with the School of Automation and Electrical Engineering, University of Science and Technology Beijing. He is a committee member and a Vice Chairman of the Younger Committee, Illuminating Engineering Society of Beijing. He is also identified as a committee member and a Deputy Secretary-General of the Man-Machine-Environment System Engineering Professional Committee, China System Engineering Institute. He has published more than 50 articles as the first author or the corresponding author and has been granted ten patents as the first inventor. His main research fields include image processing, pattern recognition, and sensor application.

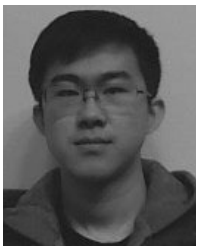

**JIACHENG LI** received the B.S. degree from the School of Automation and Electrical Engineering, University of Science and Technology Beijing, in 2018. He is currently pursuing the M.S. degree. His current research interests include image processing and laser engineering.

**YONG YANG** is currently with the department of the State Key Laboratory of Transient Optics and Photonics, Xi'an Institute of Optics and Precision Mechanics, Chinese Academy of Sciences, Xi'an, China. His research interests include application of ultrafast laser processing, development of ultrafast laser processing equipment, and laser inducing surface on materials and its application.

**JINHUI LAN** received the Ph.D. degree from the Beijing Institute of Technology, Beijing, China, in 1998. In 1998, she joined Tsinghua University, Beijing, as a Lecturer. From August 2002 to February 2004, she was a Visiting Academic with Deakin University, Geelong, Australia, working on multisensor systems. Since 2008, she has been a Professor with the School of Automation and Electrical Engineering, University of Science and Technology Beijing, China. From February 2013 to August 2013, she was a Visiting Scholar with the University of Wisconsin–Madison, Madison, WI, USA. In cooperation with other researchers, she has successfully completed more than 30 projects and solved some key technical problems. She is the author or coauthor of over 80 refereed papers in image processing, measurement and instrument, and multisensor data fusion.

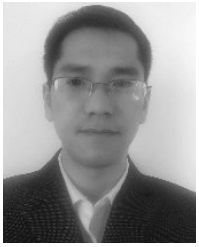

**YAFEI XUE** received the Ph.D. degree in material physics and chemistry from Beihang University, in 2014. From 2014 to 2017, he was an Engineer with the Photoelectric Technology Laboratory, Beijing Institute of Space Control Instruments. Since 2018, he has been a Senior Engineer with the Guangdong Welding Institute. He is the author of more than 13 articles and six inventions. His research interests include laser cleaning, laser welding, and laser-material interaction.